Mitochondrial dysfunction

compromises ciliary homeostasis

in astrocytes

Olesia Ignatenko[1], Satu Malinen[1], Helena Vihinen[2], Joni Nikkanen[3], Aleksandr Kononov[4], Eija Jokitalo[2], Gulayse Ince-Dunn[1,#], Anu Suomalainen[1,5,6#].

[1] Stem Cells and Metabolism Research Program, Faculty of Medicine, University of Helsinki, 00290 Helsinki, Finland

[2] Institute of Biotechnology, University of Helsinki, 00014 Helsinki, Finland

[3] Cardiovascular Research Institute, University of California, 94143-0795 San Francisco, USA

[4] Cancer Research UK, University of Manchester, SK10 4TG Manchester, UK

[5] Neuroscience Center, University of Helsinki, 00290 Helsinki, Finland

[6] HUSlab, Helsinki University Hospital, 00290 Helsinki, Finland

[#] Co-corresponding authors

Correspondence:

Prof. Anu Suomalainen Wartiovaara; anu.wartiovaara@helsinki.fi; @AWartiovaara

Ad. Prof. Gulayse Ince-Dunn gulayse.dunn@helsinki.fi; @GulayseDunn

Abstract

Reactive astrogliosis is a key component of neurological diseases. However, the active roles of astrocytes in pathogenic mechanisms and the involved molecular pathways are insufficiently understood. Here, we show that mitochondrial DNA depletion in astrocytes, causing mitochondrial spongiotic encephalopathy in mice, challenges the maintenance of primary cilium, the major cellular sensory organelle, which relays external signals to intracellular pathways. We show that mitochondrial respiratory chain deficiency in astrocytes induces FOXJ1 and RFX transcription factors, the master regulators of motile ciliogenesis, and consequently an aberrant nuclear expression program of motile cilia components. While the astrocytes still retain their single primary cilia, these organelles elongate and become remarkably distorted. Yet, respiratory chain deficiency in multiciliated ependymal cells does not cause overt cilia morphology defects. Collectively, our evidence points to an active signaling axis between astrocyte mitochondria and primary cilia. Furthermore, our data introduce metabolic ciliopathy as a pathomechanism for mitochondria-related neurodegenerative diseases.

Introduction

Astrocytes are essential for the homeostasis of the central nervous system (CNS), maintaining ionic balance, blood-brain barrier integrity, synapse function, and the metabolic homeostasis (Sofroniew and Vinters, 2010; Wang and Bordey, 2008). When stressed by disease, injury or metabolic insults, astrocytes transition into a state termed reactive astrogliosis, characterized by considerable functional, morphological, and molecular remodeling. For example, reactive astrocytes contribute to inflammatory and vascular responses, scar tissue formation, and metabolic support of the CNS cells. Depending on the insult, these responses may be protective or toxic (Anderson et al., 2016; Bush et al., 1999; Liddelow et al., 2017; Yun et al., 2018). Despite the essential functions of astrocytes in CNS metabolism, the molecular programs induced by metabolic distress remain insufficiently understood.

Mitochondrial dysfunction is a hallmark of neurodegeneration, characteristic for primary mitochondrial diseases (Gorman et al., 2016) and also secondarily implicated in common neurological diseases, such as Parkinson's and Alzheimer's diseases, amyotrophic lateral sclerosis, and Huntington's disease (Lin and Beal, 2006; Wang et al., 2019). Primary mitochondrial diseases manifest, however, with a large variation of different disease entities, indicating that mitochondrial mechanisms underlying neurological disease manifestations depend on the type of dysfunction and may be cell-type-specific. Elucidation of pathophysiological mechanisms in primary mitochondrial models is important to understand the variable roles of mitochondria for neurodegeneration in general.

Recent data highlighted astrocytes as drivers of pathogenesis of mitochondrial spongiotic brain diseases, typical for children's devastating and incurable encephalopathies (Ignatenko et al., 2018). Intriguingly, mitochondrial respiratory dysfunction specifically in astrocytes induced reactive astrogliosis, which was sufficient to drive severe brain pathology in mice (Ignatenko et al., 2018, 2020; Murru et al., 2019). Loss of mitochondrial DNA helicase Twinkle (*Twnk)* in astrocytes (TwKO[astro]) and consequent progressive depletion of mitochondrial DNA (mtDNA)

led to pervasive reactive astrogliosis starting after two months of age, with progressive vacuolation of brain parenchyma, consequent reactive microgliosis and myelin disorganisation, leading to premature death (Ignatenko et al., 2018). The brain pathology of TwKO^{astro} mice closely resembled human spongiotic encephalopathies caused by mtDNA maintenance defects (Kollberg et al., 2006; Palin et al., 2012). In contrast, *Twnk*-KO in cortical neurons was tolerated until seven months of age, after which the mice manifested with an acute-onset neurodegenerative disease (Ignatenko et al., 2018). The brain of TwKO^{astro} mice underwent metabolic reprogramming, including the induction of a mitochondrial integrated stress response (ISR^{mt}) (Ignatenko et al., 2020). This reprogramming resembled those described in other tissues and models, but all of these responses also showed some tissue- or cell-type specific components (Tyynismaa et al., 2010; Richter et al., 2013; Bao et al., 2016; Nikkanen et al., 2016; Khan et al., 2017; Kühl et al., 2017; Forsström et al., 2019; Murru et al., 2019; Mick et al., 2020). This response was not induced in neurons with the same insult. Considering the major metabolic functions of astrocytes in the nervous system, their responses to metabolic stress are of high interest.

Here we report a detailed characterization of the molecular responses of astrocytes to mtDNA depletion, using astrocytes purified from the cerebral cortex of adult TwKO^{astro} and wild-type mice. Most surprisingly, we uncover an anomalous induction of a motile ciliogenesis program, which corresponds to multiciliated cell differentiation mediated by transcription factors RFX (Regulatory Factor X) family and FOXJ1 (Forkhead Box J1). Astrocytes possess primary cilia (Kasahara et al., 2014; Sipos et al., 2018; Sterpka and Chen, 2018), but little is known about ciliary functions in neurodegeneration. Our findings of a major ciliogenic response to mitochondrial respiratory dysfunction in astrocytes constitute an exciting new front for astrocyte research in the context of brain pathologies with primary or secondary mitochondrial dysfunction, and special relevance for spongiotic encephalopathies of children.

Results and discussion

Astrocytes lacking Twinkle helicase have mtDNA depletion and induce stress responses

Using TwKO^{astro} mice as a model for mitochondrial spongiotic encephalopathies, we previously demonstrated extensive reactive astrogliosis as a response to mtDNA replication deficiency (Ignatenko et al., 2018). Here we uncovered gene expression responses to such mitochondrial dysfunction specifically in astrocytes. We purified cortical astrocytes from 3-3.5 months old TwKO^{astro} mice, using magnetic beads coated with antibodies against astrocyte-specific surface antigen ATP1B1 (ACSA-2) (Batiuk et al., 2017). At this age, TwKO^{astro} mice show early-stage disease, with mild gliosis and sparse vacuoles in brain parenchyma (Fig. S1), but advanced pathological changes, such as myelin disorganisation or neuronal loss, are not yet observed (Ignatenko et al., 2018). Astrocytes were enriched in the ACSA-2$^+$ fraction, as assessed by RT-qPCR analysis of cell-type-specific markers (Fig. 1A). Astrocytes from TwKO^{astro} mice showed a profound mtDNA depletion, which was not detectable in total brain lysates (Fig. 1B). Unsupervised principal component analysis showed that control and TwKO^{astro} samples clustered separately (Fig. 1C). Expression levels of 1,131 genes were upregulated and 408 were downregulated ($|\log_2(FC)|>0.3$ and q-value<0.1) (Fig. 1D). As a consequence of mtDNA depletion, mitochondrially encoded transcripts were among the most down-regulated (Fig. 1D, E). These results provided a proof of principle that the purified fraction represented *Twnk* knockout astrocyte population with mtDNA depletion.

A closer examination of cellular stress response genes revealed that several defining components of ISR^{mt} were induced in astrocytes purified from TwKO^{astro}: activating transcription factors (*Atf3*, *Atf5*) and *Trib3* kinase that govern the response; mitochondrial folate metabolism genes (*Mthfd2, Mthfd1l*); *Asns* that catalyses conversion of aspartate to asparagine, and the metabolic hormone *Gdf15* (Fig. 1D, F). Among other components of ISR^{mt}, we previously reported the induction of serine biosynthesis (*Psat*, *Phgdh*) and transsulfuration (*Cth*, *Cbs*) pathways in cortical lysates of 5 months old TwKO^{astro} mice (Ignatenko et al., 2020). However, these pathways were not yet induced at 3-3.5 months timepoint in either purified astrocytes or cortical lysates of TwKO^{astro} mice (Fig. 1D, (Ignatenko et al., 2020)). The stage-wise induction of ISR^{mt} mimics the skeletal muscle response in a mouse model expressing a dominant Twinkle

mutation (Forsström et al., 2019). However, the components are partially different in the two tissues: for example, FGF21, a major regulator and endocrine signaler of ISR^{mt} in the muscle, is not part of the astrocyte response. Overall, different reports (Bao et al., 2016; Kühl et al., 2017; Mick et al., 2020; Murru et al., 2019; Nikkanen et al., 2016; Richter et al., 2013; Tyynismaa et al., 2010) indicate the cell-type specificity of the ISR^{mt} components, reflecting the variable metabolic needs of the affected cell type.

We then examined the expression of genes that were reported as markers of reactive astrogliosis in various brain pathologies (Suppl. Table 1), (Escartin et al., 2021; Liddelow et al., 2017; Zamanian et al., 2012). Out of 56 such genes, expression levels of 19 were upregulated and three were downregulated in TwKO^{astro} (Fig. 1G). Genes encoding intermediate filaments and factors involved in immune responses, such as transcription factors of the NFAT family (nuclear factor of activated T cells; *Nfatc2* and *Nfatc4)*, were most robustly upregulated in our dataset (Fig. 1G). Together, the pattern established the profile of reactive astrogliosis in response to mitochondrial pathology.

Mitochondrial dysfunction in astrocytes induces a ciliogenic program

Intriguingly, the top five upregulated pathways in astrocytes purified from TwKO^{astro} mice processes were related to ciliary functions (Fig. 2A). Cilia are microtubule-based organelles that face the cell surface. Motile cilia facilitate liquid movement at the surface of lumen-facing cells, while a primary (immotile, signalling) cilium is a protrusion of plasma membrane specialized to sense and integrate external signals critical for cell proliferation and differentiation. The majority of differentiated eukaryotic cells, including astrocytes, possess a primary cilium (Dahl, 1963; Karlsson, 1966; Kasahara et al., 2014; Sterpka and Chen, 2018). Surprisingly, the ciliary pathways upregulated in TwKO^{astro} astrocytes were related to motile cilia (Fig. 2A). To analyse the expression of ciliary genes in TwKO^{astro} dataset, we used SysClia and CiliaCarta databases (van Dam et al., 2013, 2019). The expression of 64 out of 280 and 163 out of 791 genes in these gene sets was upregulated in our dataset, while only four and 13 genes were

downregulated, respectively (Fig. 2B, Suppl. Table 2). These results indicated a striking and robust activation of motile ciliary program upon astrocytic mitochondrial dysfunction.

Next, we asked whether specific transcription factor (TF) consensus sequences were enriched in the promoters of genes upregulated in astrocytes from TwKO^{astro} mice (1,000 bp window centering on the transcription start sites). The analysis revealed an enrichment of motifs recognized by RFX TF family (Fig. 2C, S2B). Intriguingly, RFX1-4 TFs have been described as master regulators of ciliogenesis in a wide range of cell types (Santos and Reiter, 2008; Thomas et al., 2010). To investigate whether experimentally determined RFX binding sites were also enriched in TwKO^{astro} dataset, we used publicly available RFX1-3 ChIP-Seq datasets derived from mouse multiciliated ependymal cells (Lemeille et al., 2020). This analysis revealed that RFX binding sites were significantly over-represented in genomic regions proximal to transcription start sites of genes upregulated in TwKO^{astro} astrocytes compared to negative gene sets (Fig. 2D, Suppl. Table 3). Finally, we investigated expression levels of *Rfx* transcripts themselves. With the exception of a slight increase in *Rfx1* levels (log$_2$(FC)=0.35, *q*-value=3.0E-03), mRNA expression of RFX family members were unchanged in TwKO^{astro} dataset (Fig. 2E, S2C). We took these findings to suggest that RFX transactivation or their recruitment to promoters, rather than their mRNA expression, was activated in our astrocyte population. In summary, analyses of genes upregulated in response to mitochondrial dysfunction in astrocytes converged on an activated ciliogenic program.

Mitochondrial dysfunction in astrocytes induces expression of motile cilia components

Motivated by the activation of a ciliary response in astrocytes of TwKO^{astro} mice, we investigated expression levels of other transcription factors that control ciliogenesis. We found robust upregulation of *Trp73* and *Foxj1,* two TFs that control motile ciliogenesis and differentiation of multiciliated cells (*Trp73* log$_2$(FC)=1.15, *q*-value=5.56E-08; *Foxj1* log$_2$(FC)=1.5, *q*-value=1.02E-06) (Fig. 2F, S2C). *Trp73* encodes TP73, which triggers a downstream cascade towards multiciliated cell differentiation, including FOXJ1 (Napoli and

Flores, 2016; Nemajerova et al., 2016), and key downstream TP73 targets (*Cdkn1a, Myb, Foxj1, Ank3 and Six3*) were all upregulated in our dataset (Fig. 2F).

In the brain, only the multiciliated ependymal cells that form the ventricular wall are known to possess motile cilia (Doetsch et al., 1997; Worthington and Cathcart, 1963). FOXJ1 is a master regulator of motile ciliogenesis that works in coordination with RFX TFs and in the brain is presumed to be active only in ependymal cells (Jacquet et al., 2009; Stubbs et al., 2008; Yu et al., 2008). However, *Foxj1* expression in sorted astrocytes was markedly higher than in unsorted brain suspension both in control and TwKO^astro mice (Fig. 2G), suggesting that *Foxj1* is enriched in astrocytes and further upregulated in TwKO^astro mice (Fig. 2F, G). Next, we asked whether *Foxj1* was indeed upregulated in cortical astrocytes or only in ependymal cells, potentially co-purifying with our astrocyte isolation method. To answer this, we investigated the spatial *Foxj1* expression with RNA-fluorescence *in situ* hybridization. *Foxj1* expression in the cerebral cortices of TwKO^astro mice was markedly increased at 3.5 months of age in comparison to controls (Fig. 2H, S2D). We also observed *Foxj1*-positive puncta in the cortex of control mice, further suggesting that the expression of *Foxj1* is not restricted to ependymal cells in the brain (Fig. 2H, S2E). As expected, ependymal cells, but not subventricular zone cells, showed a strong *Foxj1* signal (Fig. 2H). Together, our evidence suggest that FOXJ1, a regulator of multiciliated cell differentiation, is not only part of a developmental program of ependymal cell differentiation, but is also expressed in the cerebral cortex of adult mice, and its expression is upregulated upon mitochondrial dysfunction in astrocytes.

To investigate the extent of activation of a motile cilia program in TwKO^astro, we curated a catalogue of genes that encode proteins that are either unique to motile cilia, unique to primary cilia or are pan-ciliary (Suppl. Table 2). Axonemes of both primary and motile cilia comprise 9 outer doublet microtubules; motile cilia also harbor a set of distinct components essential for their movement (Fig. 2I). Expression of genes that compose all key structures specific to motile cilia were induced in TwKO^astro compared to control (Fig. 2J). These included

dynein arms and the cytoplasmic factors required for their assembly; the nexin-dynein regulatory complex (nexin link) that is located between microtubule doublets; the central pair (an additional microtubule doublet); the radial spokes that protrude towards the central pair; and other factors involved in the assembly and motility of the axoneme (Fig. 2J). The expression of most genes not specific to motile cilia (primary cilia or pan-ciliary genes) were unchanged (Fig. S2F).

To conclude, mitochondrial dysfunction induces an anomalous upregulation of *Foxj1* and the motile ciliogenic program in astrocytes, a cell type that normally possesses a single primary cilium. Intriguingly, the ectopic expression of FOXJ1 in Xenopus and zebrafish is sufficient to induce formation of functionally motile cilia in cells normally devoid of these organelles (Stubbs et al., 2008; Yu et al., 2008).

Motile ciliogenesis program is specific to metabolic and growth factor-related astrocyte stress

Next, we investigated whether the induction of motile ciliogenesis and multiciliated cell differentiation program is specific to TwKO^{astro}, or if it is induced also in other astrocyte stress models (Anderson et al., 2016; Guttenplan et al., 2020; Li et al., 2019), ageing astrocytes (Boisvert et al., 2018), or other mouse models with mitochondrial dysfunction (Kühl et al., 2017). For this, we investigated the expression of 92 genes that are either specific to motile cilia or encode ciliogenic and multiciliated cell differentiation factors (Figure S2G, Suppl. Table 2). Out of these, in astrocytes purified from TwKO^{astro} mice, expression levels of 61 genes were upregulated and one gene was downregulated (Figure S2G). Heart-specific knockout of *Twnk* or other genes involved in mitochondrial genome maintenance and expression did not induce this ciliogenic program, signifying cell specificity of the response in astrocytes (Figure S2G). Cultured astrocytes inhibited for epidermal growth factor signalling (EGFR silencing or HBEGF withdrawal) displayed a robust upregulation of the motile ciliogenesis program, including induction of *Foxj1* (Figure S2G). In contrast, reactive astrocytes stimulated with pro-inflammatory IL1+TNF**a**+C1q cocktail or sorted from mice with spinal cord injury displayed

partial downregulation of the motile ciliogenesis program (Figure S2G). Finally, astrocytes sorted from aged mouse brain showed no changes (Figure S2G). These data suggest that mitochondrial communication with cilia is cell-type specific and this function is remodelled in mitochondrial dysfunction.

Astrocytic cilia are elongated and contorted in TwKO^{astro} mice

The robust upregulation of the motile multiciliary program in *Twnk* knockout astrocytes prompted us to ask whether morphology of primary cilia, motile cilia or both, were altered in TwKO^{astro} mice. At the preterminal stage of TwKO^{astro} mice (4.5-5 months), the spongiotic pathology is advanced and reactive astrocytes are abundant (Fig. S1, (Ignatenko et al., 2018)). These reactive GFAP⁺ astrocytes were monociliated, as determined by immunofluorescent detection of the cilia axoneme protein ARL13B (Fig. 3A). We also co-stained ARL13B with another astrocytic marker, ALDH1L1 and analyzed cilia length and morphology (Fig. 3B). Our analysis revealed a shift in length distribution towards longer cilia in TwKO^{astro} mice: the range was 2.0 - 6.5 μm in controls and 2.5 - 8.2 μm in TwKO^{astro} cortex (Fig. 3C). Length distribution of cilia in reactive GFAP⁺ astrocytes were similar to ALDH1L1⁺ astrocytes of TwKO^{astro} mice (Fig. 3C).

Further, we observed that cilia morphology varies in cortical astrocytes, which we classified as straight, bent or contorted (Fig. 3D). Contorted cilia in TwKO^{astro} included S-shaped and corkscrew-like morphologies, and occasionally the long cilia appeared to form several loops (Fig. 3F, bottom panel). Such extreme morphologies never occurred in control mice. Generally, the proportion of cilia with contorted morphology was higher in TwKO^{astro} compared to control (Fig. 3E). Finally, among factors responsive to primary cilia signaling, the expression of the sonic hedgehog pathway effector *Gli1* was induced in astrocytes sorted from TwKO^{astro} mice (Fig. S2F). These results indicate that mitochondrial dysfunction in astrocytes remarkably modifies the structure of the primary signalling organelle of the cells, the cilium.

Ependymal cells remain multiciliated upon mitochondrial dysfunction

Next, we asked whether mitochondrial dysfunction also affected the morphology of motile cilia of multiciliated ependymal cells. Initially, using the Rosa26-CAG-LSL-tdTomato reporter mice, we determined that GFAP-73.12-Cre driver line used to generate TwKO^{astro} mice was active in ependymal cells (Fig. S3A). These cells in 5-month-old TwKO^{astro} mice showed a marked deficiency of the activity of cytochrome c oxidase (the respiratory chain complex IV, partially encoded by mtDNA), whereas the activity of fully nuclear-encoded complex II was preserved, similarly to the findings in cortical astrocytes of TwKO^{astro} mice (Fig. S3B, (Ignatenko et al., 2018)). Anti-ARL13B immunostaining indicated that the general morphology of ciliary tufts was preserved in TwKO^{astro} mice (Fig. 4A). Scanning electron microscopy also revealed normal ciliation across the ventricular wall (Fig. 4B). These results indicate that the aberrant ciliary structure was specific to primary cilia in astrocytes and that TwKO^{astro} had no apparent effects to motile cilia of the ependymal cells of the lateral ventricle wall.

Mitochondrial dysfunction in astrocytes alters brain lipid metabolism

Finally, gene ontology analysis of genes whose expression was reduced in astrocytes sorted from TwKO^{astro} mice, indicated changes in lipid metabolic pathways (four out of the top ten downregulated pathways) including cholesterol biosynthesis (Fig. S4A). Analysis of lipids and lipid-like molecules in an untargeted metabolomics dataset (Ignatenko et al., 2020) from TwKO^{astro} cortical lysates showed two ceramides and a cholesteryl ester depleted at the early 2.3-month-old timepoint, while in 3.2-month-old TwKO^{astro} mice 106 out of 172 identified lipid metabolites were changed (Fig. S4B, Suppl. Table 4). Specifically, the majority of identified steroids and derivatives, fatty acids and other fatty acyls, as well as prenol lipids were decreased; and sphingolipids, glycerolipids, and glycerophospholipids were imbalanced in amounts (Fig. S4B). Prominent changes were reflected also in lipid storage: ultrastructural analysis and biochemical detection with BODIPY$^{493/503}$ probe revealed an accumulation of lipid droplets in TwKO^{astro} mice at the preterminal stage (five to eight months of age) (Fig. S4C, D). Recent reports propose that astrocytes import and metabolise, via mitochondrial fatty acid oxidation, lipids generated by neurons (Ioannou et al., 2019; Liu et al., 2015, 2017). A likely

cause of accumulating of lipids in astrocytes is their impaired beta-oxidation in the absence of oxidative phosphorylation and lipid droplets serving as a protective mechanism against lipotoxicity as previously suggested (Liu et al., 2015; Nguyen et al., 2017). Collectively, our data demonstrate that mitochondrial dysfunction in astrocytes induces a severe, progressive defect in brain lipid metabolism.

In conclusion, we show here that primary mitochondrial dysfunction in astrocytes induces structural aberration of primary cilia, the cellular antenna-like protrusions and hubs for nutrient and growth signaling. Our evidence indicates that these respiratory chain deficient astrocytes induce an anomalous expression of a motile cilia program (Figure 4), governed by transcription factors FOXJ1, and the RFX family. Despite the multiciliary program induction, TwKO astrocytes had single cilia, but their structure was elongated and sometimes extremely contorted. As underlying, potentially overlapping, mechanisms we propose 1) physical constraints to accommodate very long cilia in a dense intracellular environment; 2) anomalously and chronically induced motile cilia factors trafficked to the primary cilium modifying the structure of the axoneme; 3) impaired turnover of ciliary proteins, as a consequence of ISR^{mt}, a chronic anabolic stress response to mitochondrial dysfunction.

The signaling axis between mitochondria and cilia has been recently suggested in studies of cultured cells, after toxin-mediated or genetic mitochondrial dysfunction (Bae et al., 2019; Failler et al., 2020) (Burkhalter et al., 2019). Our *in vivo* evidence indicates that metabolic stress from mitochondrial respiratory chain dysfunction leads to a genetic rewiring of the ciliary pathway in differentiated cells. The potential signals include components of ISR^{mt}, involving changes to levels of many critical metabolites such as amino acids, TCA cycle intermediates and nucleotides (Nikkanen et al., 2016), and anabolic metabolism related to ISR^{mt}. Furthermore, here we show a major dysregulation of the astrocyte lipid profile as a result of defective mitochondrial fatty acid oxidation. If and how these candidate metabolites and lipids signal to induce a ciliogenic response will no doubt be the focus of future studies. These findings open completely new avenues for investigating metabolic ciliopathy as a contributor to

pathophysiology of primary mitochondrial brain diseases of children and have potential relevance also for neurodegenerative pathologies associated with secondary mitochondrial dysfunction.

Figure legends

Fig.1: mtDNA depletion in astrocytes leads to cellular stress responses.

(A) Enrichment of cell-specific genes in ACSA-2$^+$ fraction compared to unsorted suspension, measured using RT-qPCR. Genes of interest are normalised to *Hmbs*.

(B) MtDNA amount, normalised to nuclear DNA. Measured using qPCR.

(C) Transcriptome of astrocytes, principal component (PC) analysis.

(D) Transcriptome of astrocytes, all identified genes. Gene symbols in the volcano plot denote those most downregulated genes that are encoded in the mtDNA and those most upregulated genes that are ISR^{mt} components (red dots indicate *p*-value < 0.01).

(E) Heatmap of mtDNA transcripts.

(F) Transcripts encoding ISR^{mt} components (gene list is curated based on (Forsström et al., 2019)).

(G) Transcripts that mark reactive astrogliosis (gene list is curated based on (Escartin et al., 2021; Liddelow et al., 2017; Zamanian et al., 2012)). See also Suppl. Table 1.

(C-H): RNA sequencing, astrocytes purified from Ctrl (n=6) and TwKO^{astro} (n=5) mouse brain cortical preparations, 3-3.5 months old mice. See also Suppl. Table 6. FC = fold change; ISR^{mt} = mitochondrial integrated stress response; ACSA-2 = astrocyte cell surface antigen-2; qPCR = quantitative polymerase chain reaction; RT-qPCR = real-time qPCR.

Fig.2: Mitochondrial dysfunction in astrocytes sorted from TwKO^{astro} mice induces motile ciliogenesis program.

(A-F, J): RNA sequencing, astrocytes purified from TwKO^{astro} compared to control mice. The dataset is described in Fig. 1.

(A) Gene ontology pathway enrichment analysis of upregulated genes in astrocytes of TwKO[astro] mice. Pathways involved in cilia motility are marked in red.

(B) Genes expressing ciliary proteins in astrocytes of TwKO[astro] mice (SysCilia Gold Standard gene list (van Dam et al., 2019)). See also Fig. S2A and Suppl. Table 2.

(C) Motif enrichment analysis of promoters of upregulated genes in TwKO[astro] astrocytes reveal RFX consensus motif (RFX3 motif enrichment is shown here, see also Fig. S2B).

(D) Distribution graphs of the TF binding sites proximal to the promoters of upregulated genes (ChIP-seq data from (Lemeille et al., 2020)). X-axis represents distance from TSS (transcription starting site), which equals point zero. Randomly selected gene sets either from the whole mouse genome or genes expressed in astrocytes, but not changed in our dataset, constitute negative gene sets. See also Suppl. Table 3.

(E) Transcription factors that regulate ciliogenesis in the brain; mRNA levels in TwKO[astro] astrocytes.

(F) Key steps of multiciliated cell differentiation, from cell cycle exit to motile cilia formation; schematic representation (left). The expression of the key regulators of cilia biogenesis in astrocytes of TwKO[astro] mice.

(G) *Foxj1* expression in purified astrocytes (ACSA-2^{+} fraction) compared to unsorted cell suspension; RT-qPCR, normalised to *Ywhaz* transcript level. Symbols represent individual preparations. *p*-values calculated using unpaired two-tailed parametric *t*-test.

(H) *Foxj1* expression; RNA-fluorescence *in situ* hybridization, 3.5 months old mice. Dashed lines indicate the ependymal cell layer. Puncta specific for *Foxj1* channel were analysed (arrows). Puncta that overlap with autofluorescence or ARL13B signal (arrowhead) were excluded as non-specific signal. Mice also express AAV-gfaABC1D-Arl13b-eGFP to visualize cilia. See also Fig. S2D-E.

(I) Schematic representation of cilia cross-section. Axonemes of both primary and motile cilia comprise nine doublet microtubules. Motile cilia also harbor components that are not present in primary cilia.

(J) Expression of structural components specific to motile cilia and other factors involved in axoneme assembly and motility in astrocytes of TwKO^{astro} mice compared to control mice.

Fig.3: Astrocyte cilia elongate and become contorted upon astrocytic mitochondrial dysfunction.

(A-F): Cerebral cortex, 4.5-5 months old mice.

(A-B) Ciliary marker ARL13B immunostaining in GFAP$^+$ (A) or ALDH1L1$^+$ (B) astrocytes in control and TwKO^{astro} mice.

(C) Length distribution of cilia in TwKO^{astro} and control mice. ARL13B signal in ALDH1L1$^+$ or GFAP$^+$ cells analysed. n=5 mice per genotype, 6 fields of view per mouse. Total number of cilia: control ALDH1L1$^+$, ARL13B$^+$ = 148; TwKO^{astro} ALDH1L1$^+$, ARL13B$^+$ = 174; TwKO^{astro} GFAP$^+$, ARL13B$^+$ = 75; control GFAP$^+$, ARL13B$^+$ cells were too few for analysis. Control vs TwKO^{astro} (ALDH1L1$^+$ARL13B$^+$): Kolmogorov-Smirnov test p-value < 0.0001, D = 0.5703; one-way analysis of variance: Pr (>F) = 6.76e-09. Dots represent individual cilia.

(D) Representative images of cilia morphology in control mice. Immunostaining against ARL13B.

(E) Cilia are contorted and elongated in TwKO^{astro} mice, immunostaining against ARL13B.

(F) Quantification of cilia morphology in TwKO^{astro} and control astrocytes, based on the dataset from (C). Dots represent an average per mouse. Pie charts show average per genotype.

Fig. 4. Ependymal cilia do not show apparent abnormalities upon mitochondrial dysfunction

(A-B): Cerebral cortex, 4.5-5 months old mice.

(A) Ependymal cell layer (dashed lines) with astrocytes (GFAP$^+$) and motile cilia (ARL13B$^+$).

(B) Tufts of cilia (red arrows) on the surface of ependymal cells. Scanning electron microscopy from ventricle side.

(C) Mechanistic summary: Mitochondrial dysfunction induces a ciliogenic program in astrocytes. In a healthy setting, primary cilia are assembled during brain development upon cell cycle exit, and maintained in mature astrocytes. RFX factors regulate assembly of both primary and motile cilia, while FOXJ1 and TP73 are required for ependymal cell differentiation and formation of

motile cilia. Mitochondrial dysfunction results in atypical *Foxj1* induction in cortical astrocytes, coupled with expression of motile cilia components and contorted cilia morphology.

Supplementary tables.

Suppl. Table 1. Reactive astrogliosis markers.

Suppl. Table 2. Cilia genes.

Suppl. Table 3. ChIP-Seq analysis.

Suppl. Table 4. Lipids and lipid-like molecules.

Suppl. Table 5. Oligonucleotides used in the study.

Suppl. Table 6. RNA sequencing TwKO^astro vs Control purified adult astrocytes.

Author contribution

O.I., G.I.D., and A.S. conceived and conceptualized the research. O.I. designed, planned and executed all main experiments, analysed and interpreted data. S.M. executed experiments, analysed and interpreted data. O.I., A.K., J.N., G.I.D executed and interpreted bioinformatic analyses. A.K. provided expertise for statistical analyses. H.V., E.J supervised electron microscopy experiments. O.I. assembled figures and wrote the first draft of the manuscript. O.I., G.I.D. and A.S. wrote the manuscript, and all authors commented. G.I.D. and A.S. supervised the study.

Acknowledgements

Materials and Methods

Animal experimentation

Animal experiments were approved by The National Animal Experiment Review Board and Regional State Administrative Agency for Southern Finland, following the European Union Directive. Mice were maintained in a vivarium with 12-h light:dark cycle at 22 °C and allowed access to food and water *ad libitum*. TwKO^astro mice (Ignatenko et al., 2018) (Gfap73.12Cre^+;*Twnk*^loxp/loxp mice) were generated by breeding mice carrying floxed *Twnk* alleles (Twnk^loxp/loxp or Twnk^+/loxp) to Gfap73.12-Cre^+ mice (JAX: 012886) creating a deletion of exons 2 and 3 of *Twnk*. Littermates were used as controls. Twnk^loxp/+, Twnk^loxp/loxp, Gfap73.12Cre^+;*Twnk*^loxp/+, Gfap73.12Cre^+;*Twnk*^+/+ were used as controls. The methodology for generating *Twnk*^loxp/loxp mice is previously described (Nikkanen et al., 2016). These mice carried Y508C mutation in the targeted *Twnk* gene (Nikkanen et al., 2016). Using the same method as in (Nikkanen et al., 2016), for this study we regenerated *Twnk*^loxp/loxp mice without the Y508C mutation. Gfap73.12Cre^+;*Twnk*^loxp/loxp and Gfap73.12-Cre^+;*Twnk*^Y508C/Y508C mice were indistinguishable in mtDNA brain pathology and were used interchangeably as TwKO^astro. Cre reporter mice were generated using Ai14 tdTomato mice (JAX: 007914). Mice on C57Bl/6OlaHsd or mixed genetic background mice were used. For all experiments mice were either terminally anesthetized by intraperitoneal injection of pentobarbital or were euthanized with CO_2.

Astrocyte sorting from adult mice

Astrocytes were purified using magnetic beads coated with the ACSA-2 antibody, similar to manufacturer's instructions and as previously described (Batiuk et al., 2017; Holt et al., 2019). Cerebral cortex samples from four mice per sorting preparation were dissected. Tissue was

dissociated using an enzymatic kit (Adult Brain Dissociation (P) Kit, Miltenyi Biotec, #130-107-677). Myelin debris were depleted using Myelin Removal Beads II (Miltenyi Biotec, #130-096-731). Astrocyte fraction was enriched using Anti-ACSA-2 MicroBead Kit (Miltenyi Biotec, #130-097-679).

Brain collection for histological analyses

Mice were transcardially perfused with ice-cold PBS followed by perfusion with ice-cold 4 % formaldehyde solution in PBS. The brains were postfixed in 4 % formaldehyde solution in PBS overnight at 4 °C. For immunofluorescence, brains were stored in PBS with 0.02 % sodium azide at 4 °C and then for several days incubated in 30 % sucrose in PBS solution before freezing. For RNA-fluorescence *in situ* hybridisation, after postfixing brains were transferred to 30 % sucrose in PBS for several days at 4 °C, and then frozen. Freezing was done in embedding media (O.C.T. compound Tissue-Tek #4583) at -20 °C. The brain sections were made using Thermo Scientific Cryostar NX70 cryostat at 12-20 μm to adhesive microscope slides (Matsunami Glass #TOM-11) or ThermoFisher Scientific (J1800BMNZ).

Immunofluorescence

Mouse brain sections or coverslips with cultured astrocytes were incubated in 10 % horse serum, 0.1 % Triton X-100 (or 1.0 % Tween20) in PBS for one hour at room temperature. Samples were then incubated overnight at +4 °C with primary antibodies diluted in the same solution or in an antibody diluent (Agilent #S3022). The samples were then washed in 0.1 % Triton X-100 or 1.0 % Tween20 in PBS for 30-60 minutes. Samples were then incubated for one hour at room temperature with secondary antibodies conjugated with Alexa Fluor fluorescent probes (Thermo Fisher Scientific) diluted in 10 % horse serum, 0.1 % Triton X-100 or 1.0 % Tween20 in PBS and mounted with DAPI-containing mounting medium (Vectashield #H-1200-10). Images were acquired using the Andor Dragonfly spinning disk confocal microscope. Maximum intensity projection images are presented in figure panels. Images were also acquired with a Zeiss Axio Imager epifluorescent microscope. For all images, only linear adjustments were applied. Antibodies used in the study: anti-GFAP (Sigma-Aldrich AB5804,

1:500 for mouse brain sections, 1:1000 for cultured cells); anti-Arl13b (Abcam #AB136648, 1:500 for mouse brain sections, 1:1000 for cultured cells; anti-Arl13b (Proteintech #17711-1-AP, 1:1000 for cultured cells). Maximum intensity projections of confocal images are shown.

RNA-fluorescence *in situ* hybridisation

Frozen mouse brain sections were dehydrated with ethanol, and hybridised with a probe against mouse *Foxj1* according to the manufacturer's instructions (ACD Systems #317091, #323110 and PerkinElmer #FP1487001KT, #FP1488001KT). Images were acquired using Andor Dragonfly spinning disk confocal microscope, 4 µm stacks with a 1 µm step were acquired. Signal was manually quantified from maximum intensity projection images using Fiji software by an investigator blind to genotypes. Clusters of a minimum of three puncta were quantified. The signal was quantified from three fields of view per mouse. Maximum intensity projections of confocal images are shown.

Lipid staining

To visualise lipid droplets on mouse brain sections, BODIPY$^{493/503}$ dye (intrinsic affinity to neutral and non-polar lipids) was used according to manufacturer's instructions (Thermo Fisher Scientific #D3922). Mice were transcardially perfused with ice-cold PBS, followed by perfusion with ice-cold 4 % formaldehyde solution. Brains were postfixed overnight, incubated for several days in 30 % sucrose and frozen in the embedding media and sectioned. Sections were incubated for 10 minutes in PBS, 10-60 minutes in BODIPY solution (1:100-1:1000 of the stock solution in PBS), washed twice for five minutes in PBS, mounted, and imaged.

Analysis of cilia morphology

Cilia morphology was analysed on images acquired with Andor Dragonfly spinning disk confocal microscope (7 µm stacks with a 0.5 µm step) using Imaris 9.5.1 software with Surfaces module. Settings for surfaces were adjusted to automatically detect cilia, which was followed by manual selection of surfaces of interest. Arl13b$^+$ signal in Aldh1l1$^+$ cells was analysed. Object oriented bounding box length C length was used as a proxy of ciliary length. Categories of

morphology of cilia were assigned manually, using three-dimensional images. Cilia were analysed from six fields of view per mouse.

Transmission electron microscopy

Mice were euthanised using CO_2. 1-2 mm^3 pieces of cortex were dissected out and fixed overnight at 4 °C with 2.5 % glutaraldehyde (EM-grade, Sigma-Aldrich cat. G7651) in 0.1 M sodium phosphate buffer, pH 7.4. After washing, samples were post-fixed with 1% non-reduced osmium tetroxide in 0.1 M sodium phosphate buffer for 1 h at room temperature, dehydrated in ethanol series and acetone prior to gradual infiltration into Epon (TAAB 812, Berks, UK). After polymerization at 60 °C for 18 h, ultrathin sections were cut and post-stained with uranyl acetate and lead citrate. TEM micrographs were acquired with a Jeol JEM-1400 microscope (Jeol Ltd, Tokyo, Japan) running at 80 kV using an Orius SC 1000B camera (AMETEK Gatan Inc., Pleasanton, CA, USA).

Scanning electron microscopy

Mice were transcardially perfused with ice-cold PBS followed by perfusion with ice-cold 4 % formaldehyde solution in PBS. Brains were postfixed in 2 % formaldehyde solution in 0.1 M sodium phosphate buffer for 2-6 more hours at room temperature. En-face whole-mounts of the lateral ventricle wall were dissected as previously described (Mirzadeh et al., 2010), and postfixed in 2.5 % glutaraldehyde in 0.1 M sodium phosphate buffer. Samples were stained in 2 % non-reduced osmium tetroxide in 0.1 M sodium phosphate buffer, pH 7.4 for 2 hours, dehydrated in ascending concentrations of ethanol, and dried by critical point drying (Leica EM CPD300, Leica Mikrosystems, Wetzlar, Germany). The samples were oriented using dissection microscope, mounted on aluminum stubs covered with carbon tape, and coated with a thin layer of platinum. Scanning electron microscopy micrographs were taken under high vacuum using a FEI FEG-SEM Quanta 250 (Thermo Fisher Scientific, Waltham, MA, USA) with a 5.0 kV beam, spot size 3.5.

In vivo labelling of cilia

To label cilia *in vivo* in the mouse brain, pups (P0-P5) were injected intraventricularly with AAV-gfaABC1D-Arl13b-eGFP viral vector. pAAV-ABC1D-Arl13b-eGFP plasmid was subcloned using destination vector pAAV-GFAP-GFP (addgene 50473), and a PCR-amplified insert with overhangs complimentary to destination vector from pLi3-Arl13b-eGFP plasmid (addgene 40879 (Larkins et al., 2011)). Assembly was done using NEB HiFI DNA assembly kit (NEB E5520) according to manufacturer's instructions. The plasmid was validated by direct sequencing of the insert fragment. For AAV production, the plasmid was amplified using chemically competent cells deficient for recombinase activity (Agilent Technologies #200152), purified (Macherey-Nagel #740416.10), and packaged into AAV8 vector (packaging was done by University of Helsinki AAV core unit). For injections, pups were cryoanesthetized and injections were done using stereotaxic frame as previously described (Kim et al., 2014); 2 ul per hemisphere was administered, the AAV titre was 3-3.5x10e-9 vp/µl.

In situ enzyme activity of OXPHOS Complexes

The histochemical activity assay was done as described previously (Forsström et al., 2019). Mice were euthanised with CO_2, freshly collected brains were embedded in embedding media (O.C.T. compound Tissue-Tek #4583) and frozen in 2-methylbutane bath under liquid nitrogen cooling. For simultaneous colorimetric detection of the activity of Complex IV (cytochrome-c-oxidase (COX)) and Complex II (succinate dehydrogenase (SDH)), 12 µm brain sections were incubated with enzyme substrates (30' for COX, room temperature), 40 minutes for SDH (+37 °C). COX: 0.05 M phosphate buffer (pH 7.4) with 3,3–diaminobenzidine (DAB), catalase, cytochrome *c* and sucrose. SDH: 0.05 M phosphate buffer (pH 7.4) with nitro-blue tetrazolium and sodium succinate. Sections were then dehydrated by incubations in ascending concentrations of ethanol, xylene-treated and mounted.

RT-qPCR

RNA from purified astrocytes or brain cell suspension after enzymatic digestion was extracted using RNA-binding columns (NucleoSpin RNA plus Macherey-Nagel #740984.250), genomic DNA was eliminated and cDNA was synthetised (Thermo Fisher Scientific #K1672). Real-time

quantitative PCR (RT-qPCR) reactions were performed (Bioline #BIO-98020). NCBI primer BLAST software was used for oligonucleotide design (Ye et al, 2012), 70–150 bp-long product was amplified, and oligonucleotides were designed to be separated by at least one intron of the corresponding genomic DNA of a minimum 1,000 bp length (whenever possible). Oligonucleotides for amplification of *Atp1b2*, *Slc1a3*, *Cspg4*, *Ocln* are from (Batiuk et al., 2017) and *Syt1* from (Liddelow et al., 2017). Oligonucleotide sequences can be found in Suppl. Table 5. The expression of the genes of interest was normalized to hydroxymethylbilane synthase (*Hmbs* or *Ywhaz*) expression.

mtDNA quantification

Purified astrocytes or brain tissue suspension after enzymatic digestion was lysed in TNES buffer with Proteinase K overnight at 55 °C water bath. DNA was extracted using phenol–chloroform, followed by ethanol and ammonium acetate precipitation. Pellet was washed with ethanol, dried, and resuspended in 10 mM Tris-Cl, pH 8.0. Quantitative analysis of mtDNA was performed by quantitative PCR, normalized to a nuclear gene *Rmb15* as described in (Ignatenko et al., 2020). Oligonucleotide sequences can be found in Suppl. Table 5.

Metabolomics

Metabolomics datasets are from (Ignatenko et al., 2020). All metabolites belonging to lipids and lipid-like molecules (HMDB super class) were analysed and grouped for plotting according to HMDB classification. The mice were 2.3 months old. See also Suppl. Table 4.

RNA sequencing

RNA was extracted from purified astrocyte preparations using RNA-binding columns (NucleoSpin RNA plus Macherey-Nagel #740984.250). RNA was analyzed using TapeStation, and only samples with RIN>7 were used. RNA sequencing was done in the BGI Genomics, China. mRNA was enriched by Oligo dT selection, and reverse transcription was done using random N6 primer. End repair and adaptor ligation were followed by PCR amplification of the library. The library was sequenced using BGISEQ-500 platform, paired-end sequencing, read

length 100 bp. After sequencing, reads were filtered to remove adaptor sequences, contamination, and low-quality reads using Soapnuke software version 1.6.7 version (filtering parameters -n 0.001 -l 20 -q 0.4 -A 0.25). Additionally, quality of reads was analysed using FastaQC software. The data are available in NCBI GEO repository (accession number GSE174343) (Edgar et al., 2002). See also Suppl. Table 6.

Bioinformatic analyses

Quantification of transcript abundance in RNA sequencing dataset was done using Kallisto software (mm10 build, (Bray et al., 2016)). Differential expression analysis and PCA plot were prepared with Sleuth (Pimentel et al., 2017), gene ontology pathway enrichment analysis was done with Metascape (Zhou et al., 2019). Upregulated genes: top 1000 gene were analysed (genes with q-value<0.1 and $\log_2$(FC)>0.3 were selected, and then sorted by $\log_2$(FC)). Downregulated genes: all genes with q-value<0.1 and $\log_2$(FC)<-0.3 were selected (408 genes). RNA sequencing analysis of published datasets (Suppl. Table 2): available from NCBI GEO repository (GSE76097; GSE99791; GSE96518; GSE143598; GSE125610). $\log_2$(FC) were used (Anderson et al., 2016; Boisvert et al., 2018; Guttenplan et al., 2020; Kühl et al., 2017), or $\log_2$FC were calculated from raw read counts using DeSeq2 (Li et al., 2019; Love et al., 2014).

For motif enrichment analysis (Suppl. Table 3), genomic sequences corresponding to 500 bp upstream and 500 bp downstream from the transcription start sites (TSS) of upregulated genes were extracted ($\log_2$(FC)>0.25 and p-adj-value<0.05) (mm10 build) (Yates et al., 2020). As a negative dataset, 1,000 randomly selected genes from the mouse genome were used. To find enriched motifs CentriMo tool from the MEME Suite was used (Bailey and Machanick, 2012). For analysis of TF binding site enrichment, genomic coordinates for binding sites of RFX1-3 based on a previously published ChIP-Seq study were used (Lemeille et al., 2020). Genomic coordinates spanning 10,000 bp upstream and 10,000 bp downstream from TSSs of upregulated genes ($\log_2$(FC)>0.25 and p-adj-value<0.01) were extracted. An overlay of the two datasets in Excel revealed the RFX binding sites within TSS proximal sequences of upregulated genes. As negative datasets either randomly selected genes from the mouse genome or genes

which were expressed in astrocytes but not changed based on our RNA-Seq results were used. GRCm38 (mm10) mouse genome build was used for all analyses and manipulations on genomic intervals were carried out using the Galaxy platform (Afgan et al., 2018).

Statistical analysis

Statistical analyses were performed using Prism 8 software and R; graphs were made with Prism 8. Statistical analysis of differential gene expression of RNA sequencing data generated in this study was done using the Sleuth package (Pimentel et al., 2017), q-values were used throughout the study to determine statistical significance of these comparisons. Statistical analyses of the cilia length distribution were done using Kolmogorov-Smirnov test in Prism 8 and ANOVA test in R base software. Statistical analysis of cilia morphology and RNA-fluorescence *in situ* hybridization between two groups was performed using unpaired two-tailed parametric *t* test in Prism 8. Heatmaps were generated using Complex Heatmap package in R (Gu et al., 2016), Z-scores were calculated from scaled reads per base.

References

Afgan, E., Baker, D., Batut, B., van den Beek, M., Bouvier, D., Cech, M., Chilton, J., Clements, D., Coraor, N., Grüning, B.A., et al. (2018). The Galaxy platform for accessible, reproducible and collaborative biomedical analyses: 2018 update. Nucleic Acids Res. *46*, W537–W544.

Anderson, M.A., Burda, J.E., Ren, Y., Ao, Y., O'Shea, T.M., Kawaguchi, R., Coppola, G., Khakh, B.S., Deming, T.J., and Sofroniew, M.V. (2016). Astrocyte scar formation aids central nervous system axon regeneration. Nature *532*, 195–200.

Bae, J.-E., Kang, G.M., Min, S.H., Jo, D.S., Jung, Y.-K., Kim, K., Kim, M.-S., and Cho, D.-H. (2019). Primary cilia mediate mitochondrial stress responses to promote dopamine neuron survival in a Parkinson's disease model. Cell Death Dis. *10*, 952.

Bailey, T.L., and Machanick, P. (2012). Inferring direct DNA binding from ChIP-seq. Nucleic Acids Res. *40*, e128.

Bao, X.R., Ong, S.-E., Goldberger, O., Peng, J., Sharma, R., Thompson, D.A., Vafai, S.B., Cox, A.G., Marutani, E., Ichinose, F., et al. (2016). Mitochondrial dysfunction remodels one-carbon metabolism in human cells. Elife *5*.

Batiuk, M.Y., de Vin, F., Duqué, S.I., Li, C., Saito, T., Saido, T., Fiers, M., Belgard, T.G., and

Holt, M.G. (2017). An immunoaffinity-based method for isolating ultrapure adult astrocytes based on ATP1B2 targeting by the ACSA-2 antibody. J. Biol. Chem. *292*, 8874–8891.

Boisvert, M.M., Erikson, G.A., Shokhirev, M.N., and Allen, N.J. (2018). The Aging Astrocyte Transcriptome from Multiple Regions of the Mouse Brain. Cell Rep. *22*, 269–285.

Bray, N.L., Pimentel, H., Melsted, P., and Pachter, L. (2016). Near-optimal probabilistic RNA-seq quantification. Nat. Biotechnol. *34*, 525–527.

Burkhalter, M.D., Sridhar, A., Sampaio, P., Jacinto, R., Burczyk, M.S., Donow, C., Angenendt, M., Competence Network for Congenital Heart Defects Investigators, Hempel, M., Walther, P., et al. (2019). Imbalanced mitochondrial function provokes heterotaxy via aberrant ciliogenesis. J. Clin. Invest. *129*, 2841–2855.

Bush, T.G., Puvanachandra, N., Horner, C.H., Polito, A., Ostenfeld, T., Svendsen, C.N., Mucke, L., Johnson, M.H., and Sofroniew, M.V. (1999). Leukocyte infiltration, neuronal degeneration, and neurite outgrowth after ablation of scar-forming, reactive astrocytes in adult transgenic mice. Neuron *23*, 297–308.

Dahl, H.A. (1963). Fine structure of cilia in rat cerebral cortex. Z. Zellforsch. Mikrosk. Anat. *60*, 369–386.

van Dam, T.J., Wheway, G., Slaats, G.G., SYSCILIA Study Group, Huynen, M.A., and Giles, R.H. (2013). The SYSCILIA gold standard (SCGSv1) of known ciliary components and its applications within a systems biology consortium. Cilia *2*, 7.

van Dam, T.J.P., Kennedy, J., van der Lee, R., de Vrieze, E., Wunderlich, K.A., Rix, S., Dougherty, G.W., Lambacher, N.J., Li, C., Jensen, V.L., et al. (2019). CiliaCarta: An integrated and validated compendium of ciliary genes. PLoS One *14*, e0216705.

Doetsch, F., García-Verdugo, J.M., and Alvarez-Buylla, A. (1997). Cellular composition and three-dimensional organization of the subventricular germinal zone in the adult mammalian brain. J. Neurosci. *17*, 5046–5061.

Edgar, R., Domrachev, M., and Lash, A.E. (2002). Gene Expression Omnibus: NCBI gene expression and hybridization array data repository. Nucleic Acids Res. *30*, 207–210.

Escartin, C., Galea, E., Lakatos, A., O'Callaghan, J.P., Petzold, G.C., Serrano-Pozo, A., Steinhäuser, C., Volterra, A., Carmignoto, G., Agarwal, A., et al. (2021). Reactive astrocyte nomenclature, definitions, and future directions. Nat. Neurosci.

Failler, M., Giro-Perafita, A., Owa, M., Srivastava, S., Yun, C., Kahler, D.J., Unutmaz, D., Esteva, F.J., Sánchez, I., and Dynlacht, B.D. (2020). Whole-genome screen identifies diverse pathways that negatively regulate ciliogenesis. Mol. Biol. Cell mbcE20020111.

Forsström, S., Jackson, C.B., Carroll, C.J., Kuronen, M., Pirinen, E., Pradhan, S., Marmyleva, A., Auranen, M., Kleine, I.-M., Khan, N.A., et al. (2019). Fibroblast Growth Factor 21 Drives Dynamics of Local and Systemic Stress Responses in Mitochondrial Myopathy with mtDNA Deletions. Cell Metab. *30*, 1040-1054.e7.

Gorman, G.S., Chinnery, P.F., DiMauro, S., Hirano, M., Koga, Y., McFarland, R., Suomalainen, A., Thorburn, D.R., Zeviani, M., and Turnbull, D.M. (2016). Mitochondrial diseases. Nat Rev Dis Primers *2*, 16080.

Gu, Z., Eils, R., and Schlesner, M. (2016). Complex heatmaps reveal patterns and correlations in multidimensional genomic data. Bioinformatics *32*, 2847–2849.

Guttenplan, K.A., Weigel, M.K., Adler, D.I., Couthouis, J., Liddelow, S.A., Gitler, A.D., and Barres, B.A. (2020). Knockout of reactive astrocyte activating factors slows disease progression in an ALS mouse model. Nat. Commun. *11*, 3753.

Holt, L.M., Stoyanof, S.T., and Olsen, M.L. (2019). Magnetic Cell Sorting for In Vivo and In Vitro Astrocyte, Neuron, and Microglia Analysis. Curr. Protoc. Neurosci. *88*, e71.

Ignatenko, O., Chilov, D., Paetau, I., de Miguel, E., Jackson, C.B., Capin, G., Paetau, A., Terzioglu, M., Euro, L., and Suomalainen, A. (2018). Loss of mtDNA activates astrocytes and leads to spongiotic encephalopathy. Nat. Commun. *9*, 70.

Ignatenko, O., Nikkanen, J., Kononov, A., Zamboni, N., Ince-Dunn, G., and Suomalainen, A. (2020). Mitochondrial spongiotic brain disease: astrocytic stress and harmful rapamycin and ketosis effect. Life Sci Alliance *3*.

Ioannou, M.S., Jackson, J., Sheu, S.-H., Chang, C.-L., Weigel, A.V., Liu, H., Amalia Pasolli, H., Shan Xu, C., Pang, S., Matthies, D., et al. (2019). Neuron-Astrocyte Metabolic Coupling Protects against Activity-Induced Fatty Acid Toxicity. Cell *177*, 1522-1535.e14.

Jacquet, B.V., Salinas-Mondragon, R., Liang, H., Therit, B., Buie, J.D., Dykstra, M., Campbell, K., Ostrowski, L.E., Brody, S.L., and Ghashghaei, H.T. (2009). FoxJ1-dependent gene expression is required for differentiation of radial glia into ependymal cells and a subset of astrocytes in the postnatal brain. Development *136*, 4021–4031.

Karlsson, U. (1966). Three-dimensional studies of neurons in the lateral geniculate nucleus of the rat. I. Organelle organization in the perikaryon and its proximal branches. J. Ultrastruct. Res. *16*, 429–481.

Kasahara, K., Miyoshi, K., Murakami, S., Miyazaki, I., and Asanuma, M. (2014). Visualization of astrocytic primary cilia in the mouse brain by immunofluorescent analysis using the cilia marker Arl13b. Acta Med. Okayama *68*, 317–322.

Khan, N.A., Nikkanen, J., Yatsuga, S., Jackson, C., Wang, L., Pradhan, S., Kivelä, R., Pessia, A.,

Velagapudi, V., and Suomalainen, A. (2017). mTORC1 Regulates Mitochondrial Integrated Stress Response and Mitochondrial Myopathy Progression. Cell Metab. *26*, 419-428.e5.

Kim, J.-Y., Grunke, S.D., Levites, Y., Golde, T.E., and Jankowsky, J.L. (2014). Intracerebroventricular viral injection of the neonatal mouse brain for persistent and widespread neuronal transduction. J. Vis. Exp. 51863.

Kollberg, G., Moslemi, A.-R., Darin, N., Nennesmo, I., Bjarnadottir, I., Uvebrant, P., Holme, E., Melberg, A., Tulinius, M., and Oldfors, A. (2006). POLG1 mutations associated with progressive encephalopathy in childhood. J. Neuropathol. Exp. Neurol. *65*, 758–768.

Kühl, I., Miranda, M., Atanassov, I., Kuznetsova, I., Hinze, Y., Mourier, A., Filipovska, A., and Larsson, N.-G. (2017). Transcriptomic and proteomic landscape of mitochondrial dysfunction reveals secondary coenzyme Q deficiency in mammals. Elife *6*.

Larkins, C.E., Aviles, G.D.G., East, M.P., Kahn, R.A., and Caspary, T. (2011). Arl13b regulates ciliogenesis and the dynamic localization of Shh signaling proteins. Mol. Biol. Cell *22*, 4694–4703.

Lemeille, S., Paschaki, M., Baas, D., Morlé, L., Duteyrat, J.-L., Ait-Lounis, A., Barras, E., Soulavie, F., Jerber, J., Thomas, J., et al. (2020). Interplay of RFX transcription factors 1, 2 and 3 in motile ciliogenesis. Nucleic Acids Res.

Li, J., Khankan, R.R., Caneda, C., Godoy, M.I., Haney, M.S., Krawczyk, M.C., Bassik, M.C., Sloan, S.A., and Zhang, Y. (2019). Astrocyte-to-astrocyte contact and a positive feedback loop of growth factor signaling regulate astrocyte maturation. Glia *67*, 1571–1597.

Liddelow, S.A., Guttenplan, K.A., Clarke, L.E., Bennett, F.C., Bohlen, C.J., Schirmer, L., Bennett, M.L., Münch, A.E., Chung, W.-S., Peterson, T.C., et al. (2017). Neurotoxic reactive astrocytes are induced by activated microglia. Nature *541*, 481–487.

Lin, M.T., and Beal, M.F. (2006). Mitochondrial dysfunction and oxidative stress in neurodegenerative diseases. Nature *443*, 787–795.

Liu, L., Zhang, K., Sandoval, H., Yamamoto, S., Jaiswal, M., Sanz, E., Li, Z., Hui, J., Graham, B.H., Quintana, A., et al. (2015). Glial lipid droplets and ROS induced by mitochondrial defects promote neurodegeneration. Cell *160*, 177–190.

Liu, L., MacKenzie, K.R., Putluri, N., Maletić-Savatić, M., and Bellen, H.J. (2017). The Glia-Neuron Lactate Shuttle and Elevated ROS Promote Lipid Synthesis in Neurons and Lipid Droplet Accumulation in Glia via APOE/D. Cell Metab. *26*, 719-737.e6.

Love, M., Anders, S., and Huber, W. (2014). Differential analysis of count data--the DESeq2 package. Genome Biol. *15*, 10–1186.

Mick, E., Titov, D.V., Skinner, O.S., Sharma, R., Jourdain, A.A., and Mootha, V.K. (2020). Distinct mitochondrial defects trigger the integrated stress response depending on the metabolic state of the cell. ELife *9*.

Mirzadeh, Z., Doetsch, F., Sawamoto, K., Wichterle, H., and Alvarez-Buylla, A. (2010). The subventricular zone en-face: wholemount staining and ependymal flow. J. Vis. Exp.

Murru, S., Hess, S., Barth, E., Almajan, E.R., Schatton, D., Hermans, S., Brodesser, S., Langer, T., Kloppenburg, P., and Rugarli, E.I. (2019). Astrocyte-specific deletion of the mitochondrial m-AAA protease reveals glial contribution to neurodegeneration. Glia *67*, 1526–1541.

Napoli, M., and Flores, E.R. (2016). Unifying the p73 knockout phenotypes: TAp73 orchestrates multiciliogenesis. Genes Dev. *30*, 1253–1254.

Nemajerova, A., Kramer, D., Siller, S.S., Herr, C., Shomroni, O., Pena, T., Gallinas Suazo, C., Glaser, K., Wildung, M., Steffen, H., et al. (2016). TAp73 is a central transcriptional regulator of airway multiciliogenesis. Genes Dev. *30*, 1300–1312.

Nguyen, T.B., Louie, S.M., Daniele, J.R., Tran, Q., Dillin, A., Zoncu, R., Nomura, D.K., and Olzmann, J.A. (2017). DGAT1-Dependent Lipid Droplet Biogenesis Protects Mitochondrial Function during Starvation-Induced Autophagy. Dev. Cell *42*, 9-21.e5.

Nikkanen, J., Forsström, S., Euro, L., Paetau, I., Kohnz, R.A., Wang, L., Chilov, D., Viinamäki, J., Roivainen, A., Marjamäki, P., et al. (2016). Mitochondrial DNA Replication Defects Disturb Cellular dNTP Pools and Remodel One-Carbon Metabolism. Cell Metab. *23*, 635–648.

Palin, E.J.H., Hakonen, A.H., Korpela, M., Paetau, A., and Suomalainen, A. (2012). Mitochondrial recessive ataxia syndrome mimicking dominant spinocerebellar ataxia. Journal of the Neurological Sciences *315*, 160–163.

Pimentel, H., Bray, N.L., Puente, S., Melsted, P., and Pachter, L. (2017). Differential analysis of RNA-seq incorporating quantification uncertainty. Nature Methods *14*, 687–690.

Richter, U., Lahtinen, T., Marttinen, P., Myöhänen, M., Greco, D., Cannino, G., Jacobs, H.T., Lietzén, N., Nyman, T.A., and Battersby, B.J. (2013). A mitochondrial ribosomal and RNA decay pathway blocks cell proliferation. Curr. Biol. *23*, 535–541.

Santos, N., and Reiter, J.F. (2008). Building it up and taking it down: the regulation of vertebrate ciliogenesis. Dev. Dyn. *237*, 1972–1981.

Sipos, É., Komoly, S., and Ács, P. (2018). Quantitative comparison of primary cilia marker expression and length in the mouse brain. J. Mol. Neurosci. *64*, 397–409.

Sofroniew, M.V., and Vinters, H.V. (2010). Astrocytes: biology and pathology. Acta Neuropathol. *119*, 7–35.

Sterpka, A., and Chen, X. (2018). Neuronal and astrocytic primary cilia in the mature brain. Pharmacol. Res. *137*, 114–121.

Stubbs, J.L., Oishi, I., Izpisúa Belmonte, J.C., and Kintner, C. (2008). The forkhead protein Foxj1 specifies node-like cilia in Xenopus and zebrafish embryos. Nat. Genet. *40*, 1454–1460.

Thomas, J., Morlé, L., Soulavie, F., Laurençon, A., Sagnol, S., and Durand, B. (2010). Transcriptional control of genes involved in ciliogenesis: a first step in making cilia. Biol. Cell *102*, 499–513.

Tyynismaa, H., Carroll, C.J., Raimundo, N., Ahola-Erkkilä, S., Wenz, T., Ruhanen, H., Guse, K., Hemminki, A., Peltola-Mjøsund, K.E., Tulkki, V., et al. (2010). Mitochondrial myopathy induces a starvation-like response. Hum. Mol. Genet. *19*, 3948–3958.

Wang, D.D., and Bordey, A. (2008). The astrocyte odyssey. Prog. Neurobiol. *86*, 342–367.

Wang, Y., Xu, E., Musich, P.R., and Lin, F. (2019). Mitochondrial dysfunction in neurodegenerative diseases and the potential countermeasure. CNS Neurosci. Ther. *25*, 816–824.

Worthington, W.C., Jr, and Cathcart, R.S., 3rd (1963). Ependymal cilia: distribution and activity in the adult human brain. Science *139*, 221–222.

Yates, A.D., Achuthan, P., Akanni, W., Allen, J., Allen, J., Alvarez-Jarreta, J., Amode, M.R., Armean, I.M., Azov, A.G., Bennett, R., et al. (2020). Ensembl 2020. Nucleic Acids Res. *48*, D682–D688.

Yu, X., Ng, C.P., Habacher, H., and Roy, S. (2008). Foxj1 transcription factors are master regulators of the motile ciliogenic program. Nat. Genet. *40*, 1445–1453.

Yun, S.P., Kam, T.-I., Panicker, N., Kim, S., Oh, Y., Park, J.-S., Kwon, S.-H., Park, Y.J., Karuppagounder, S.S., Park, H., et al. (2018). Block of A1 astrocyte conversion by microglia is neuroprotective in models of Parkinson's disease. Nature Medicine *24*, 931–938.

Zamanian, J.L., Xu, L., Foo, L.C., Nouri, N., Zhou, L., Giffard, R.G., and Barres, B.A. (2012). Genomic analysis of reactive astrogliosis. J. Neurosci. *32*, 6391–6410.

Zhou, Y., Zhou, B., Pache, L., Chang, M., Khodabakhshi, A.H., Tanaseichuk, O., Benner, C., and Chanda, S.K. (2019). Metascape provides a biologist-oriented resource for the analysis of systems-level datasets. Nat. Commun. *10*, 1523.
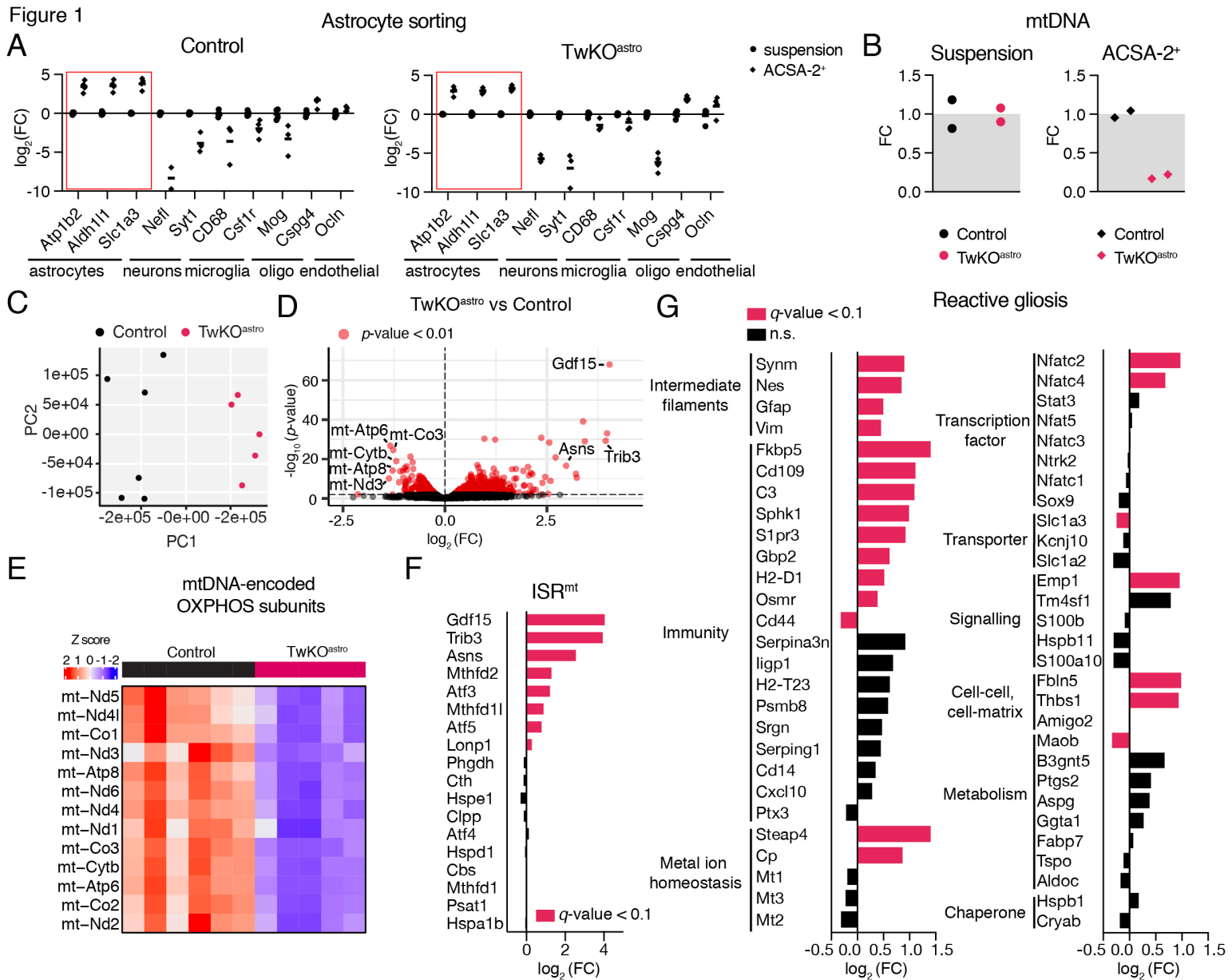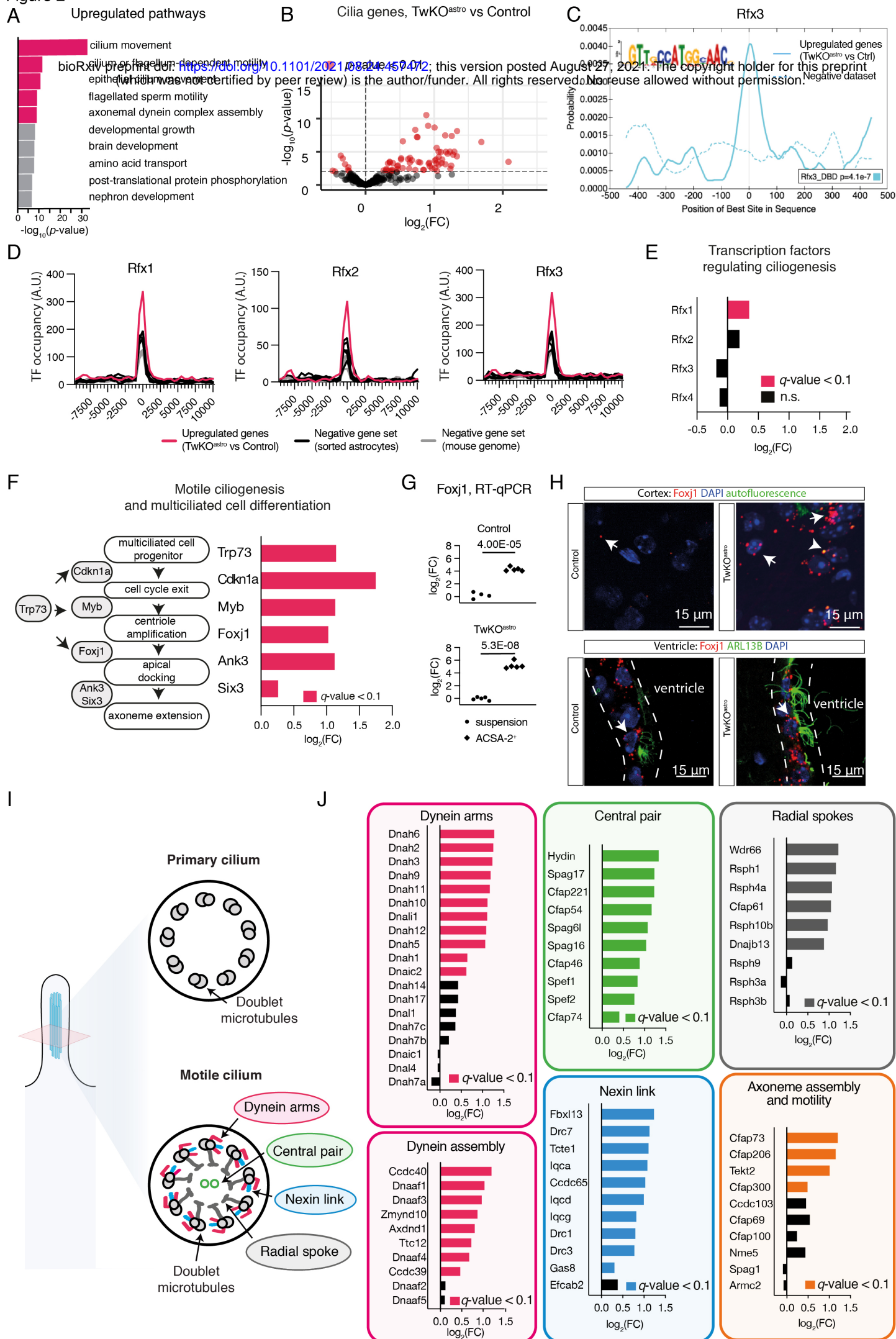
Figure 1

Figure 2

A Upregulated pathways

B Cilia genes, TwKO^astro vs Control

C Rfx3

D Rfx1 — Rfx2 — Rfx3

TF occupancy (A.U.)

Upregulated genes (TwKO^astro vs Control) — Negative gene set (sorted astrocytes) — Negative gene set (mouse genome)

E Transcription factors regulating ciliogenesis

q-value < 0.1 — n.s.

F Motile ciliogenesis and multiciliated cell differentiation

multiciliated cell progenitor → cell cycle exit → centriole amplification → apical docking → axoneme extension

Trp73, Cdkn1a, Myb, Foxj1, Ank3, Six3

q-value < 0.1

G Foxj1, RT-qPCR

Control — TwKO^astro

suspension — ACSA-2^+

H Cortex: Foxj1 DAPI autofluorescence

Ventricle: Foxj1 ARL13B DAPI

I Primary cilium — Motile cilium

Doublet microtubules — Dynein arms — Central pair — Nexin link — Radial spoke

J Dynein arms — Central pair — Radial spokes — Dynein assembly — Nexin link — Axoneme assembly and motility

Figure 3

Figure 4